AGU PUBLICATIONS

JGR

Journal of Geophysical Research: Space Physics

TECHNIQUE

10.1002/2013JA019734

Key Points:
- A data assimilation approach is applied for modeling the plasmasphere
- The proposed technique allows us to estimate the evolution of He+ distribution
- The parameter for the profile along a field line could also be estimated

Correspondence to:
S. Nakano,
shiny@ism.ac.jp

Citation:
Nakano, S., M.-C. Fok, P. C. Brandt, and T. Higuchi (2014), Estimation of temporal evolution of the helium plasmasphere based on a sequence of IMAGE/EUV images, *J. Geophys. Res. Space Physics*, *119*, 3708–3723, doi:10.1002/2013JA019734.

Received 23 DEC 2013
Accepted 19 APR 2014
Accepted article online 25 APR 2014
Published online 15 MAY 2014

Estimation of temporal evolution of the helium plasmasphere based on a sequence of IMAGE/EUV images

S. Nakano[1,2,3], M.-C. Fok[4], P. C. Brandt[5], and T. Higuchi[1,2]

[1]The Institute of Statistical Mathematics, Research Organization of Information and Systems, Tachikawa, Tokyo, Japan, [2]School of Multidisciplinary Sciences, The Graduate University for Advanced Studies, Hayama, Kanagawa, Japan, [3]Department of Meteorology, University of Reading, Reading, UK, [4]NASA Goddard Space Flight Center, Greenbelt, Maryland, USA, [5]Applied Physics Laboratory, The Johns Hopkins University, Laurel, Maryland, USA

Abstract We have developed a technique for estimating the temporal evolution of the plasmaspheric helium ion density based on a sequence of extreme ultraviolet (EUV) data obtained from the IMAGE satellite. In the proposed technique, the estimation is obtained by incorporating EUV images from IMAGE into a two-dimensional fluid model of the plasmasphere using a data assimilation approach based on the ensemble transform Kalman filter. Since the motion and the spatial structure of the helium plasmasphere is strongly controlled by the electric field in the inner magnetosphere, the electric field around the plasmapause can also be estimated using the ensemble transform Kalman filter. We performed an experiment using synthetic images that were generated from the same numerical model under a certain condition. It was confirmed that the condition that generated the synthetic images was successfully reproduced. We also present some results obtained using real EUV imaging data. Finally, we discuss the possibility of estimating the density profile along a magnetic field line. Since each EUV image was taken from a different direction due to the motion of the IMAGE satellite, we could obtain the information on the density profile along a field line by combining multiple images.

1. Introduction

The plasmasphere basically corresponds to the region in which the corotation electric field is dominant over the convection field and an $E \times B$ drift path forms a closed loop. In this closed drift path region, high plasma density can be maintained because the plasma supplied from the ionosphere follows closed drift trajectories around the Earth and thus passes through the dayside ionospheric outflow region multiple times. In contrast, the plasma outside the closed drift path region would rapidly be lost due to the convection electric field. Hence, under a stationary condition, a sharp gradient in plasma density would be formed between the closed drift path region and the open drift path region. The outer boundary of the plasmasphere is defined by this sharp density gradient, which is referred to as the plasmapause [e.g., *Nishida*, 1966].

Since the motion of plasmaspheric ions is determined by the $E \times B$ drift, the structure of the plasmasphere is highly variable due to the variation of the electric field in the inner magnetosphere [e.g., *Liemohn et al.*, 2004; *Pierrard et al.*, 2008]. Moreover, since the timescale for the response to the storm-time electric field is typically much shorter than the timescale of the refilling from the ionosphere [e.g., *Park*, 1974; *Obana et al.*, 2010], the time history of the electric field would also control the structures of the plasmasphere. The electric field in the inner magnetosphere is influenced by the interaction between the ionosphere and the magnetosphere [e.g., *Vasyliunas*, 1970, 1972; *Jaggi and Wolf*, 1973; *Fok et al.*, 2001; *Liemohn et al.*, 2005]. In order to understand the dynamics of the plasmasphere as a result of the coupling processes between the ionosphere, the magnetosphere, and the plasmasphere, it is crucial to grasp the global picture of the electric field. There are efforts to provide averaged maps of the electric potential distribution [*Matsui et al.*, 2004, 2013]. However, it is difficult to obtain global, time-dependent information on the electric field in the inner magnetosphere.

The extreme ultraviolet (EUV) imager on board the IMAGE satellite [*Sandel et al.*, 2000], which observes extreme ultraviolet radiation scattered by helium ions in the plasmasphere, provides information on global motion of the helium ion plasmasphere. As pointed out by *Burch et al.* [2001b], this information could be used to estimate the electric field in the inner magnetosphere. Indeed, a number of studies have addressed the properties of the inner-magnetospheric electric field based on IMAGE/EUV data. For example,

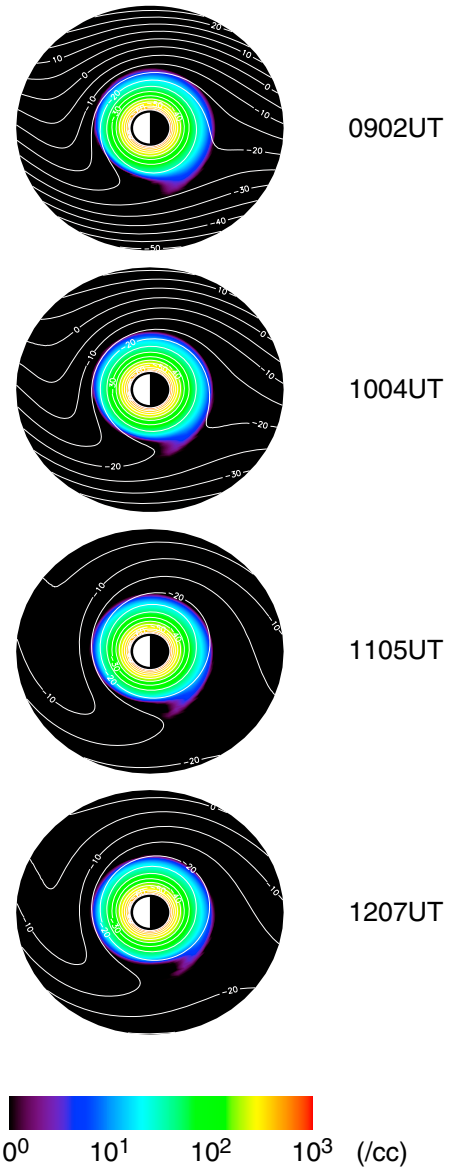

Figure 1. Modeled evolution of helium ion density for generating the synthetic EUV images. The color contours indicate the ion density, and the white lines indicate the electric potential contours with intervals of 5 kV.

Goldstein et al. [2002] inferred the overshielding electric field from the property of the shoulder structure. *Goldstein et al.* [2004] demonstrated that the azimuthal electric field might be estimated from the motion of the plasmapause location identified from the EUV data. A similar approach was taken by *Murakami et al.* [2007] to discuss the response of the plasmapause to the interplanetary magnetic field (IMF). *Goldstein et al.* [2005] investigated the radial electric field as well as the azimuthal field by tracking the azimuthal motion of an undulated structure of the plasmasphere. *Galvan et al.* [2010] also investigated the azimuthal motion of the plasmasphere from the EUV images. *Gallagher and Adrian* [2007] discussed the two-dimensional plasma flow based on the optical flow and the correlation analysis of EUV images.

The present study attempts to exploit the global EUV imaging data for estimating the temporal evolution of the plasmasphere which is controlled by the electric field. We use a data assimilation method [e.g., *Kalnay*, 2003] to attain this purpose. Data assimilation is an approach which incorporates observations into a simulation model to obtain a realistic estimate of the temporal evolution of a system. Simulation models in geophysics are typically based on many untested assumptions regarding the initial condition, model parameters, and so on. Data assimilation methods make use of real observations of the system in order to reduce the errors arising from these assumptions. The initial condition, unknown model parameters, and the simulation variables at each time step are improved so that the simulation outputs well agree with the observations. Recently, data assimilation has been applied to a number of targets of the magnetosphere. In particular, many studies performed data assimilation for modeling of the radiation belt [e.g., *Naehr and Toffoletto*, 2005; *Koller et al.*, 2007; *Kondrashov et al.*, 2007; *Boudarie and Maget*, 2012]. *Nakano et al.* [2008] used a data assimilation approach to model the dynamics of the ring current using the data of the energetic neutral atom (ENA) from the IMAGE satellite. For the plasmasphere, *Jorgensen et al.* [2011] demonstrated the capabilities of data assimilation using a synthetic data set of satellite in situ observations. The present study attempts to demonstrate the effectiveness of data assimilation of global EUV imaging data for the modeling of the plasmasphere.

The EUV images provide the information on the spatial structure of the helium plasmasphere. Combining a sequence of the EUV images with the dynamical model of the plasmasphere, we can also estimate the spatial distribution of the electric potential around the plasmasphere because the temporal evolution of the helium plasmasphere is controlled by the electric field. The estimate of the helium ion distribution is also improved by considering the temporal evolution of the plasmasphere. This is a similar approach to that reported by *Nakano et al.* [2008] who modeled the ring current using the ENA data. The proposed approach consists of two steps. First, we estimate the helium ion density distribution at the initial time step of an event using a linear inversion. Second, we incorporate a sequence of IMAGE/EUV data into a dynamic model in order to estimate the electric potential distribution and the evolution of the plasmasphere controlled by the electric field.

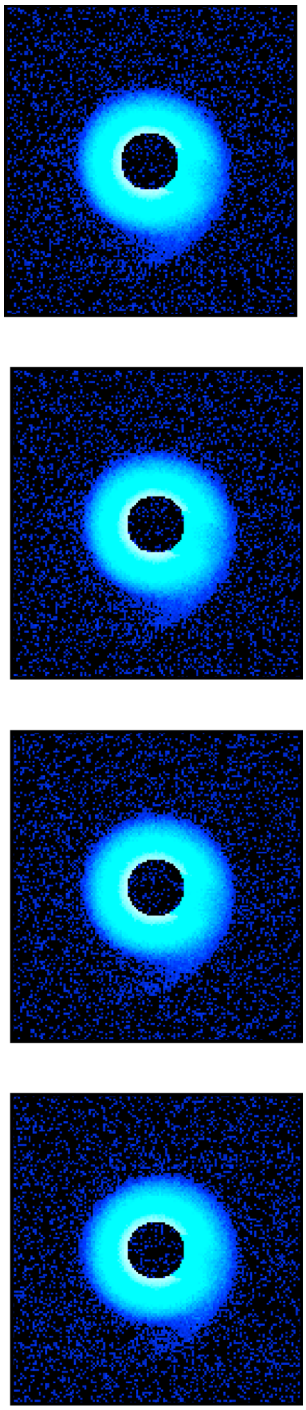

Figure 2. Synthetic EUV images used in the experiment.

The dynamic model of the plasmasphere used in the present study is explained in section 2. The method by which to estimate the evolution of helium ion density distribution and electric field estimation is described in section 3 and is validated using a synthetic data set in section 4. The results of the estimation for two real events are presented in section 5. Finally, a conclusion is presented in section 6.

2. Plasmasphere Model

We use a two-dimensional plasmasphere model based on the model developed by *Ober et al.* [1997] to describe the temporal evolution of the plasmaspheric helium ion distribution. In this model, the evolution of the ion distribution is described by the following advection equation:

$$\frac{\partial N}{\partial t} - \frac{\nabla\Phi \times \boldsymbol{B}}{B^2} \cdot \nabla N = f, \tag{1}$$

where N denotes the total ion content per unit flux tube, Φ denotes the electric potential, $\boldsymbol{B}$ denotes the magnetic field, and f represents the refilling process on the dayside and diffusive process on the nightside. Since only helium ions are considered in the present study, we hereinafter denote the helium ion content per unit flux tube by N. The helium ions were assumed to be distributed in the region $1.1 < L < 8$. In the present study, we consider phenomena with a relatively short time period of less than 6 h, and the refilling and diffusive processes are assumed to be ineffective; that is, we assume $f = 0$. Indeed, even if f was set to be 10^7 /(cm^2 · s), which is the typical value of the upward helium ion flux from the ionosphere [*Hoffman and Dodson*, 1980], the results did not show any visible changes for the cases shown in the present paper. The refilling rate would be less than the upward ion flux from the ionosphere. Therefore, it would be reasonable to assume the refilling process to be ineffective.

In order to estimate the density distribution of helium ions from an EUV image, the helium ion density profile along a field line must be given. According to a number of preceding studies [e.g., *Menk et al.*, 1999; *Denton et al.*, 2006], we assume that the profile of the helium ion density n along a field line can be written in the following power law form:

$$n(\boldsymbol{r}) = n_{\mathrm{eq}}(\boldsymbol{\rho}) \left(\frac{r_{\mathrm{eq}}}{r} \right)^{\alpha}, \tag{2}$$

where n_{eq} is the helium ion density at the equatorial plane and $\boldsymbol{\rho}$ is the projection of $\boldsymbol{r}$ along the field line on the equatorial plane. The total ion content per unit flux tube, N, can then be obtained by integrating the density along the magnetic field line m as follows:

$$N = \int_m \frac{n_{\mathrm{eq}}(\boldsymbol{\rho})}{B(\boldsymbol{r})} \left(\frac{r_{\mathrm{eq}}}{r} \right)^{\alpha} \mathrm{d}s. \tag{3}$$

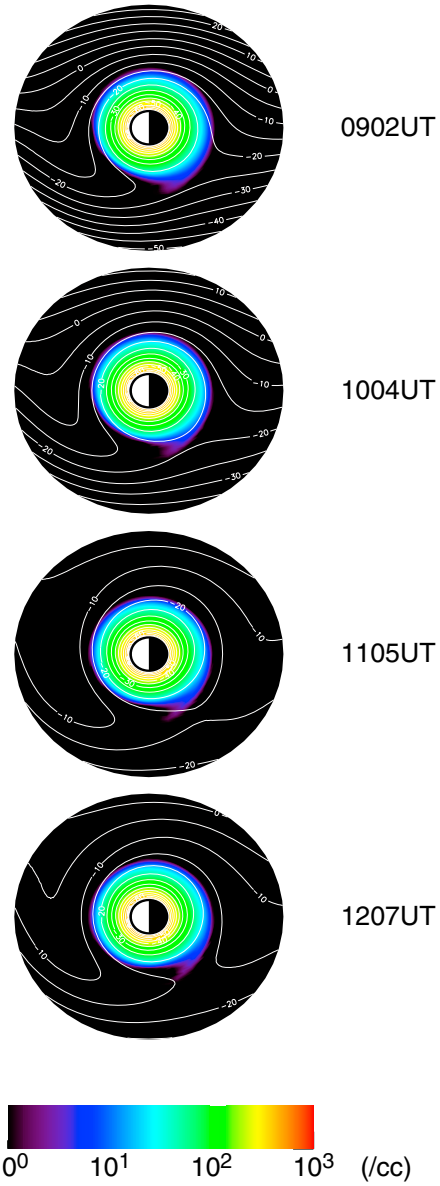

Figure 3. Evolution of the helium ion distribution (color code) and the electric potential distribution (white lines) estimated from the synthetic data set using the ETKF.

This relationship allows us to convert between N in equation (1) and the equatorial helium ion density n_{eq}. Thus, in the following, we do not consider N but consider the equatorial helium ion density n_{eq}.

We assume the magnetospheric magnetic field $\boldsymbol{B}$ to be a dipole field. On the other hand, the spatial distribution of the electric potential Φ is assumed to be unknown, and it is estimated in the data assimilation process. In order to make the estimation easier, the spatial distribution of the electric field potential at the equatorial plane is expressed as:

$$\Phi = \Phi_0 \left(\frac{\rho}{R_0}\right)^2 \sin\phi + \sum_{\substack{0\le i\le 3\\ 0\le j\le 3}} \mathcal{J}_i\left(\xi_{ij}\frac{\rho}{R_0}\right)\left(a_{ij}\cos i\phi + b_{ij}\sin i\phi\right), \tag{4}$$

where ρ is the radial distance from the Earth's center, ϕ is the magnetic local time in radians, R_0 is the equatorial radius of the outer boundary of the simulation domain, $\mathcal{J}_i$ is the ith order Bessel function, and ξ_{ij} are the positive roots of $\mathcal{J}_i(\xi_{ij}) = 0$ such that $0 < \xi_{i1} < \xi_{i2} < \cdots$. Here, the equatorial radius of the outer boundary R_0 is assumed to be 8 earth radii. By assuming equipotentiality along a magnetic field line, the electric potential at any point in the inner magnetosphere is given by that at the equatorial plane represented by equation (4).

The parameter Φ_0, which corresponds to the potential drop imposed across the polar cap, is set at the potential drop calculated from the model by *Weimer* [2001] with solar wind data obtained by the ACE as an input. The first term on the right-hand side of equation (4) corresponds to the Volland-Stern-type electric field with a shielding factor of 2. The second term is the deviation from the Volland-Stern-type electric field, which is represented by a linear combination of the basis functions $\mathcal{J}_i(\xi_{ij}\frac{\rho}{R_0})\cos i\phi$ and $\mathcal{J}_i(\xi_{ij}\frac{\rho}{R_0})\sin i\phi$ for $0 \le i \le 3$ and $0 \le j \le 3$. The second term can represent various potential patterns by changing the coefficients a_{ij} and b_{ij}. In the proposed technique, a_{ij} and b_{ij} are treated as unknown parameters. The electric potential distribution is then be estimated by seeking optimal values for the coefficients a_{ij} and b_{ij}. This is a similar approach to that in our previous study *Nakano et al.* [2008], although the equation of the electric potential distribution was slightly modified. At the outer boundary of the simulation domain, where $r = R_0$, the second term becomes zero. The outer boundary condition of the electric potential is thus determined by the Volland-Stern-type electric field model.

3. Method

3.1. State Space Representation

For convenience in explaining the proposed technique, the relationship between the variables considered herein is described in the form of the state space representation. We define a state vector $\boldsymbol{x}_k$ by gathering all the unknown variables in the plasmasphere model, which includes the equatorial helium ion density for each cell $n_{eq,j}$, and coefficients a_{ij} and b_{ij} representing the electric potential distribution. Subscript k of $\boldsymbol{x}_k$ represents the time t_k. The temporal evolution of $\boldsymbol{x}_k$ from t_{k-1} to t_k is then described as follows:

$$\boldsymbol{x}_k = \mathcal{M}_k(\boldsymbol{x}_{k-1}) + \boldsymbol{v}_k, \tag{5}$$

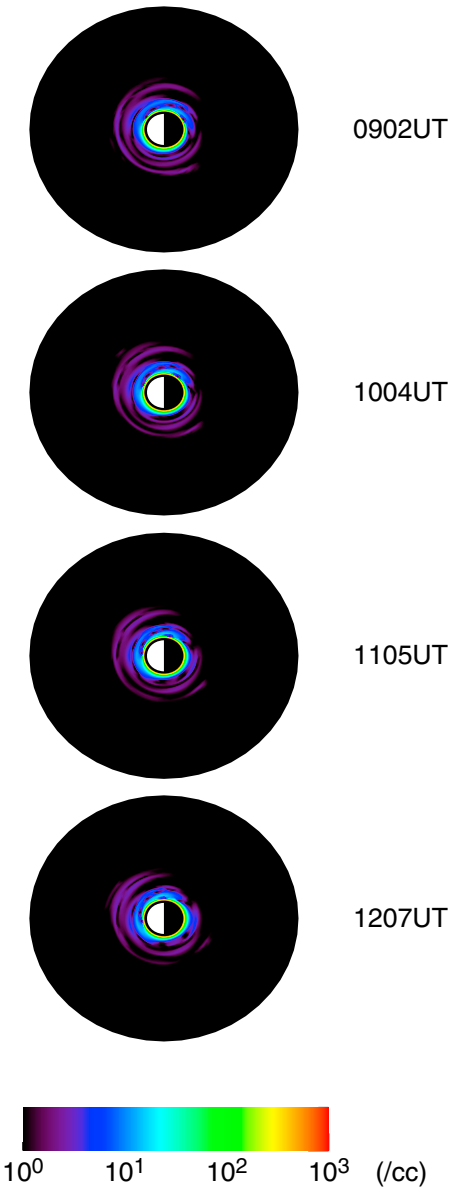

Figure 4. Absolute values of the differences in the helium ion density between the estimate in Figure 3 and the truth in Figure 1.

where $\mathcal{M}_k$ denotes the dynamic model, which describes the temporal evolution of $\boldsymbol{x}_k$, and the vector $\boldsymbol{v}_k$ is the system noise, which represents the uncertain processes that are not described by the dynamical model $\mathcal{M}_k$. The state vector $\boldsymbol{x}_k$ consists of the helium ion density $n_{\mathrm{eq},j}$ and the coefficients representing the electric potential a_{ij} and b_{ij}. Accordingly, the function $\mathcal{M}_k$ consists of the temporal evolution of N, which corresponds to equation (1), and the evolution of a_{ij} and b_{ij}. In the present study, we assume that the evolution of each of coefficients a_{ij} and b_{ij} is described by the following model:

$$a_{ij,k} = Aa_{ij,k-1}, \qquad b_{ij,k} = Ab_{ij,k-1}, \tag{6}$$

where A is fixed for all of $\{a_{ij}\}$ and $\{b_{ij}\}$. The coefficient A is a kind of forgetting factor and is set to 0.8 herein.

The EUV observation used in the present study is related to the helium ion density. Since the helium ion density is given by equation (2), the measured EUV intensity of each pixel, y_i, can be obtained by the line of sight integral of the helium ion density

$$\begin{aligned} y_i &= \int_{\ell_i} c(\boldsymbol{r})\, n_{\mathrm{eq}}(\boldsymbol{\rho}) \left(\frac{r_{\mathrm{eq}}}{r}\right)^{\alpha} \mathrm{d}s + \varepsilon_i \\ &= \int_{\ell_i} \eta(\boldsymbol{r})\, n_{\mathrm{eq}}(\boldsymbol{\rho})\, \mathrm{d}s + \varepsilon_i, \end{aligned} \tag{7}$$

where we define η as

$$\eta(\boldsymbol{r}) = c(\boldsymbol{r}) \left(\frac{r_{\mathrm{eq}}}{r}\right)^{\alpha}, \tag{8}$$

and ε_i denotes the observation noise for each pixel. In the sunlit plasmasphere, c is given according to *Gallagher et al.* [2005]:

$$c = \frac{F}{1.89 \times 10^{19}}, \tag{9}$$

where F is the 30.4 nm solar irradiance in units of photons per $\mathrm{cm}^2 \cdot \mathrm{s}$. In the umbra of the Earth, EUV scattering is assumed to be negligible, and c is assumed to be zero. We then approximate equation (7) in the following discretized form:

$$y_i = \sum_j \eta_{ij} n_{\mathrm{eq},j} + \varepsilon_i. \tag{10}$$

This equation can be rewritten in the following vector form:

$$\boldsymbol{y} = \mathrm{H}\boldsymbol{n}_{\mathrm{eq}} + \boldsymbol{\varepsilon}. \tag{11}$$

In order to represent the relationship between the state vector $\boldsymbol{x}_k$ and the observation $\boldsymbol{y}_k$, we define a matrix $\hat{\mathrm{H}}$ so as to satisfy $\hat{\mathrm{H}}\boldsymbol{x}_k = \mathrm{H}\boldsymbol{n}_{\mathrm{eq},k}$. Equation (11) can then be rewritten as follows:

$$\boldsymbol{y} = \hat{\mathrm{H}}\boldsymbol{x}_k + \boldsymbol{\varepsilon}_k. \tag{12}$$

The observation noise $\boldsymbol{\varepsilon}_k$ is assumed to obey the Gaussian distribution with the mean vector $\boldsymbol{b}$ and the covariance matrix R. The values of $\boldsymbol{b}$ and R are given in the same way as in a companion paper [*Nakano et al.*, 2014].

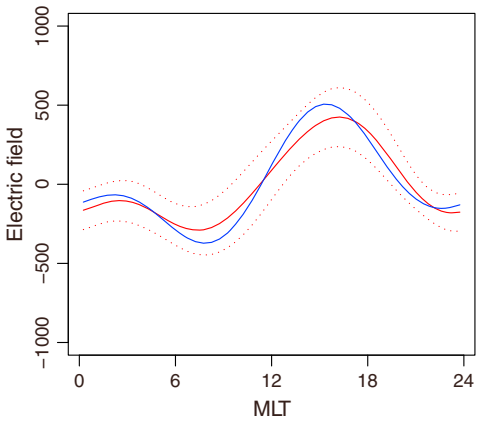

Figure 5. Eastward electric field distribution at $L = 3.5$ at 1004 UT estimated from the synthetic data set (red line) and the "true" eastward electric field (blue line).

3.2. Ensemble Transform Kalman Filter

The goal of the present study is to estimate the temporal evolution of the helium ion density distribution of the plasmasphere and the electric potential distribution using a sequence of EUV imaging data obtained from the IMAGE satellite. In order to accomplish this goal, we use the ensemble transform Kalman filter (ETKF) [*Bishop et al.*, 2001; *Wang et al.*, 2004], which is a sequential data assimilation algorithm for combining a dynamic model with a sequence of observations. In the ETKF, as in other ensemble-based methods such as the ensemble Kalman filter [*Evensen*, 1994, 2003], the probability distribution of the state $\boldsymbol{x}_k$ is represented by a set of instances called an ensemble. The evolution of uncertainty of the system is represented by applying the dynamic model $\mathcal{M}$ for each member of the ensemble. For example, if the probability distribution at the previous time step is represented by the ensemble $\left\{\boldsymbol{x}^{(1)}_{k-1|k-1}, \ldots, \boldsymbol{x}^{(N)}_{k-1|k-1}\right\}$, we can obtain the ensemble representing the forecast distribution as follows:

$$\boldsymbol{x}^{(i)}_{k|k-1} = \mathcal{M}\left(\boldsymbol{x}^{(i)}_{k-1|k-1}\right) \tag{13}$$

for all i. Here the subscript $k|k-1$ of $\boldsymbol{x}^{(i)}_{k|k-1}$ indicates that $\boldsymbol{x}^{(i)}_{k|k-1}$ represents the probability distribution for time t_k conditioned on the observations until time t_{k-1}. Similarly, the ensemble $\left\{\boldsymbol{x}^{(1)}_{k-1|k-1}, \ldots, \boldsymbol{x}^{(N)}_{k-1|k-1}\right\}$ represents the probability distribution for time t_{k-1} conditioned on the observations until time t_{k-1}. The form of equation (13) does not consider the error or uncertainty in the dynamical model, which corresponds to $\boldsymbol{v}_k$ in equation (5). In order to cope with the possible errors and uncertainties due to the processes which are not accurately described in the model, we apply the multiplicative covariance inflation [e.g., *Anderson and Anderson*, 1999] as follows:

$$\boldsymbol{x}^{(i)}_{k|k-1} = (1+\delta)\left[\mathcal{M}\left(\boldsymbol{x}^{(i)}_{k-1|k-1}\right) - \overline{\mathcal{M}(\boldsymbol{x}_{k-1|k-1})}\right] \tag{14}$$

for all i where $(1+\delta)$ is the inflation factor. In the present paper, we set $\delta = 0.1$. The mean vector and the covariance matrix of the forecast distribution can then be obtained as follows:

$$\bar{\boldsymbol{x}}_{k|k-1} = \frac{1}{N}\sum_{i=1}^{N}\boldsymbol{x}^{(i)}_{k|k-1}, \tag{15}$$

$$\mathrm{P}_{k|k-1} = \frac{1}{N}\sum_{i=1}^{N}\left(\boldsymbol{x}^{(i)}_{k|k-1} - \bar{\boldsymbol{x}}_{k|k-1}\right)\left(\boldsymbol{x}^{(i)}_{k|k-1} - \bar{\boldsymbol{x}}_{k|k-1}\right)^T. \tag{16}$$

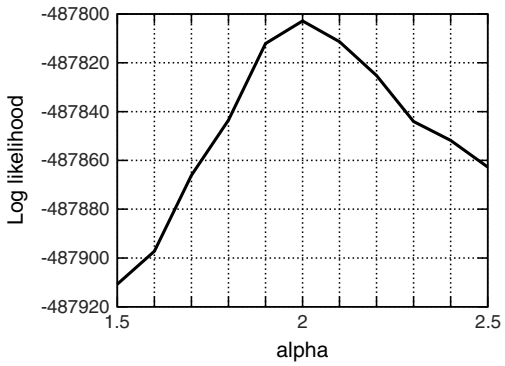

Figure 6. Log likelihood with respect to α for the synthetic data set.

where $\bar{\boldsymbol{x}}_{k|k}$ and $\mathrm{P}_{k|k}$ denote the mean vector and the covariance matrix, respectively, of the forecast. The superscript T indicates the transpose of the matrix.

For convenience, we define the following matrix:

$$\mathrm{X}_{k|k-1} = \frac{1}{\sqrt{N}}\left(\delta\boldsymbol{x}^{(1)}_{k|k-1} \quad \cdots \quad \delta\boldsymbol{x}^{(N)}_{k|k-1}\right), \tag{17}$$

where $\delta\boldsymbol{x}^{(i)}_{k|k-1}$ is the deviation from the mean $\bar{\boldsymbol{x}}_{k|k-1}$:

$$\delta\boldsymbol{x}^{(i)}_{k|k-1} = \boldsymbol{x}^{(i)}_{k|k-1} - \bar{\boldsymbol{x}}_{k|k-1}. \tag{18}$$

Using the matrix $\mathrm{X}_{k|k-1}$, the ensemble covariance matrix $\mathrm{P}_{k|k-1}$ is represented as

$$\mathrm{P}_{k|k-1} = \mathrm{X}_{k|k-1}\mathrm{X}^T_{k|k-1}. \tag{19}$$

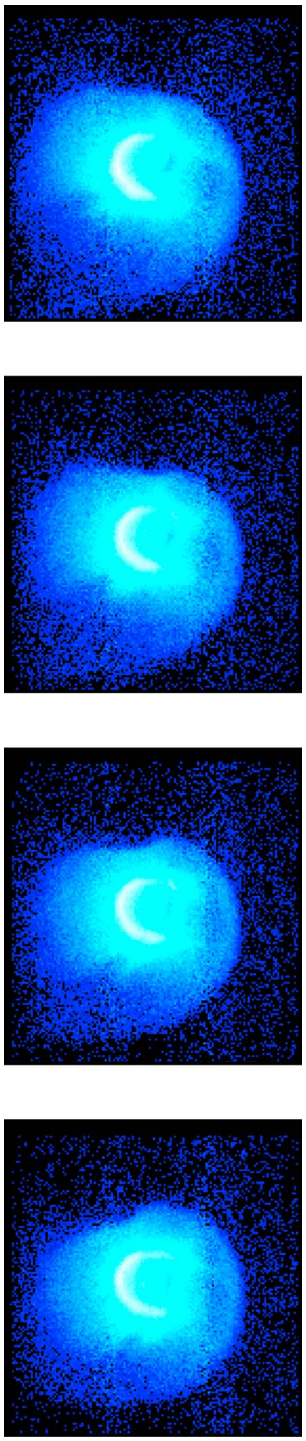

Figure 7. Sequence of EUV images for the event of 20 June 2001.

This means that $X_{k|k-1}$ is the square root of the covariance matrix $P_{k|k-1}$. In order for the mean of the particles $\left\{\boldsymbol{x}_{k|k-1}^{(1)}, \ldots, \boldsymbol{x}_{k|k-1}^{(N)}\right\}$ to be equal to $\bar{\boldsymbol{x}}_{k|k-1}$ as in equation (15), the matrix $X_{k|k-1}$ also satisfies the following condition:

$$X_{k|k-1}\mathbf{1} = \mathbf{0}, \tag{20}$$

where $\mathbf{1} = (1 \cdots 1)^T$ and $\mathbf{0} = (0 \cdots 0)^T$.

The ETKF incorporates the information of the observation $\boldsymbol{y}_k$ into the estimate based on the conventional Kalman filter algorithm [*Kalman*, 1960]. The mean vector is thus updated as follows:

$$\bar{\boldsymbol{x}}_{k|k} = \bar{\boldsymbol{x}}_{k|k-1} + K_k\left(\boldsymbol{y}_k - H_k\bar{\boldsymbol{x}}_{k|k-1} - \boldsymbol{b}\right), \tag{21}$$

where $\bar{\boldsymbol{x}}_{k|k}$ denotes the mean vector of the analysis (filtered) distribution and K_k is the Kalman gain matrix. The ETKF does not explicitly compute the covariance matrix of the analysis. Instead, the ETKF updates the square root of $P_{k|k}$ as follows:

$$X_{k|k} = X_{k|k-1}T_k, \tag{22}$$

where the transform matrix T_k is defined such that the matrix $X_{k|k}$ satisfies

$$P_{k|k} = X_{k|k}X_{k|k}^T. \tag{23}$$

In order to compute the Kalman gain matrix K_k and the transform matrix T_k, the following eigenvalue decomposition is performed:

$$X_{k|k-1}^T H_k^T R^{-1} H_k X_{k|k-1} = U_{kk}U_k^T. \tag{24}$$

We then obtain

$$K_k = X_{k|k-1}U_k(I_N + {}_k)^{-1}U_k^T X_{k|k-1}^T H_k^T R^{-1}, \tag{25}$$

$$T_k = U_k(I_N + {}_k)^{-\frac{1}{2}}U_k^T. \tag{26}$$

The right-hand side of equation (26) must be multiplied by the matrix U_k^T in order to obtain an unbiased ensemble that satisfies the following condition:

$$X_{k|k}\mathbf{1} = X_{k|k-1}T_k\mathbf{1} = \mathbf{0}, \tag{27}$$

where $\mathbf{1} = (1 \cdots 1)^T$ and $\mathbf{0} = (0 \cdots 0)^T$ [*Wang et al.*, 2004; *Livings et al.*, 2008; *Sakov and Oke*, 2008]. Finally, we decompose the matrix $X_{k|k}$:

$$\left(\delta\boldsymbol{x}_{k|k}^{(1)} \quad \cdots \quad \delta\boldsymbol{x}_{k|k}^{(N)}\right) = \sqrt{N}\,X_{k|k}. \tag{28}$$

Using the mean vector $\bar{\boldsymbol{x}}_{k|k}$, which was obtained in equation (21), we obtain the new ensemble representing the filtered distribution as follows:

$$\boldsymbol{x}_{k|k}^{(i)} = \bar{\boldsymbol{x}}_{k|k} + \delta\boldsymbol{x}_{k|k}^{(i)}. \tag{29}$$

From this ensemble, we can again obtain an ensemble representing the forecast distribution according to equation (13). The temporal evolution of the helium ion density can be estimated by applying the above procedures recursively.

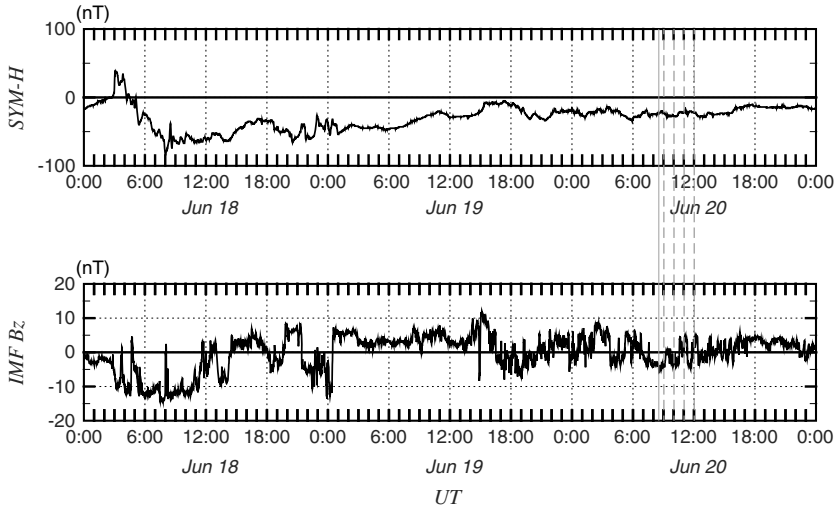

Figure 8. *SYM-H* index and the north-south component of the IMF from 0 UT on 18 June 2001 to 0 UT on 21 June 2001. The times at which the EUV images in Figure 7 were taken are indicated with vertical dashed lines.

3.3. Fixed-Lag Smoother

The above algorithm provides an estimate for $\boldsymbol{x}_k$ at each time step t_k based on the current and past observations. However, we can consider subsequent observations for the estimation of $\boldsymbol{x}_k$ using a procedure referred to as a smoother [e.g., *Evensen and van Leeuwen*, 2000]. We use a fixed-lag smoother, which can be obtained as an extension of a filtering algorithm [e.g., *Cohn et al.*, 1994]. In the fixed-lag smoother, an augmented state vector which includes the current and past states as follows:

$$\boldsymbol{x}_k^* = \begin{pmatrix} \boldsymbol{x}_k \\ \boldsymbol{x}_{k-1} \\ \vdots \\ \boldsymbol{x}_{k-\lambda} \end{pmatrix}. \tag{30}$$

The system and observation models for the augmented state vector are then defined as

$$\boldsymbol{x}_k^* = \mathcal{M}_k^* \left(\boldsymbol{x}_{k-1}^*\right) + \boldsymbol{v}_k^*, \tag{31}$$

$$\boldsymbol{y}_k^* = \hat{\mathrm{H}}_k^* \boldsymbol{x}_k^* + \boldsymbol{\varepsilon}_k^*. \tag{32}$$

Here $\mathcal{M}_k^*$ and $\hat{\mathrm{H}}_k^*$ are defined as follows:

$$\mathcal{M}_k^* \left(\boldsymbol{x}_{k-1}^*\right) = \begin{pmatrix} \mathcal{M}_k(\boldsymbol{x}_{k-1}) \\ \boldsymbol{x}_{k-1} \\ \vdots \\ \boldsymbol{x}_{k-\lambda} \end{pmatrix}, \tag{33}$$

$$\hat{\mathrm{H}}_k^* \boldsymbol{x}_k^* = \hat{\mathrm{H}}_k \boldsymbol{x}_k. \tag{34}$$

If we apply the same algorithm as the ETKF described above to the model with the augmented state vector up to λ time steps ahead, we can obtain estimates that consider the observations at subsequent λ time steps. In the present study, we estimate the state after considering two subsequent time steps by using this fixed-lag smoother.

3.4. Initial Condition

In order to apply the ETKF, the initial condition must be given in advance. We then obtain the initial state with the linear inversion of a single EUV image. The method of linear inversion is the same as that in a companion paper [*Nakano et al.*, 2014], in which we estimate the equatorial helium ion density n_{eq} using the Bayesian approach. Assuming that the prior distribution and the likelihood function

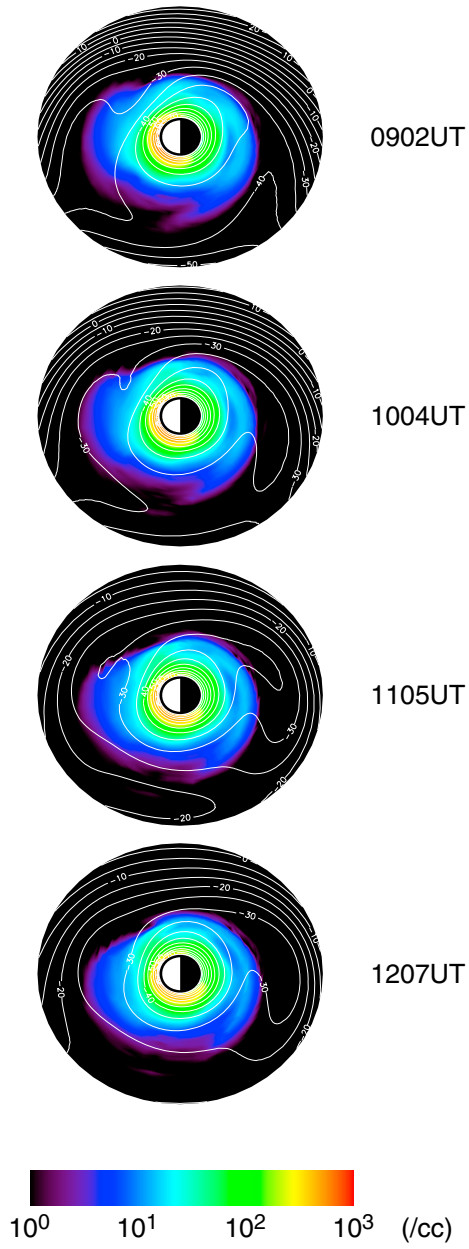

Figure 9. Estimated evolution of the helium ion distribution (color code) and the electric potential distribution (white lines) on 20 June 2001.

are Gaussian, the posterior density is maximized at the mean of the posterior distribution $\bar{\boldsymbol{n}}_{\mathrm{eq}}$, which is given as

$$\bar{\boldsymbol{n}}_{\mathrm{eq}} = (\mathrm{P}_b^{-1} + \mathrm{H}^T\mathrm{R}^{-1}\mathrm{H})^{-1}\mathrm{H}^T\mathrm{R}^{-1}(\boldsymbol{y} - \boldsymbol{b}), \tag{35}$$

where the matrix R is the covariance matrix of the observation noise $\boldsymbol{\epsilon}$, and the matrix P_b is the covariance matrix of the prior distribution. We adopt $\bar{\boldsymbol{n}}_{\mathrm{eq}}$ as the estimate. A detailed explanation of the linear inversion technique is provided in a companion paper [*Nakano et al.*, 2014]. The matrix R is assumed to be diagonal, and each of the diagonal elements is determined by the variance among the neighbor pixels. The covariance matrix of the prior distribution P_b is designed so as to satisfy the following relationship:

$$-\frac{1}{2}\boldsymbol{n}_{\mathrm{eq}}^T\mathrm{P}_b^{-1}\boldsymbol{n}_{\mathrm{eq}} = -\frac{1}{2}\sum_i L_i^2\left[\xi_L^2\left(\frac{\partial^2 n_{\mathrm{eq}}}{\partial L^2}\right)_i + \xi_\phi^2\left(\frac{\partial^2 n_{\mathrm{eq}}}{\partial \phi^2}\right)_i\right]^2, \tag{36}$$

where $L = |\boldsymbol{\rho}|$ and ϕ is the longitude. The subscript i denotes one of the cells discretizing the equatorial plane.

3.5. Parameter Estimation

In section 2, the value of the power law exponent in equation (2), α, was not specified. A number of studies have estimated α in the plasmasphere mainly for the electron density or mass density. However, the estimates in the literature vary [*Reinisch et al.*, 2009]. In particular, no reliable estimate is available regarding α for helium ion density.

In the present paper, we attempt to estimate the value of α from a sequence of EUV images. Each of the EUV images was taken from a different direction because of the motion of the IMAGE satellite. Therefore, we might be able to obtain information on the three-dimensional structure by referring to multiple images. When we estimate the helium ion density using the ETKF, we can also evaluate the fitness to the EUV observations. If the estimation is performed using various values of α, the fitness to the observations can be evaluated for each value of α. This provides a rough estimate for α. In order to measure the fitness, we introduce the likelihood of the parameter α, $p(\boldsymbol{y}_{1:K}|\alpha)$, where $\boldsymbol{y}_{1:K} = \{\boldsymbol{y}_1, \boldsymbol{y}_2, \ldots, \boldsymbol{y}_K\}$. The likelihood can be decomposed as follows:

$$p(\boldsymbol{y}_{1:K}|\alpha) = p(\boldsymbol{y}_K|\boldsymbol{y}_{1:K-1}, \alpha)\cdots p(\boldsymbol{y}_2|\boldsymbol{y}_1, \alpha)\,p(\boldsymbol{y}_1|\alpha). \tag{37}$$

The likelihood indicates the probability that the sequence of the observed data are yielded from the given probability density function with the parameter α. If we assume or approximate that all the probability distribution is Gaussian, we can compute the logarithm of the likelihood $p(\boldsymbol{y}_{1:K}|\alpha)$ using the equation for the Kalman filter [*Kitagawa*, 2010]:

$$\log p(\boldsymbol{y}_{1:K}|\alpha) \propto -\frac{1}{2}\sum_{k=1}^{K}\boldsymbol{\epsilon}_{k|k-1}^T(\mathrm{H}_k\mathrm{X}_{k|k-1}\mathrm{X}_{k|k-1}^T\mathrm{H}_k^T + \mathrm{R})^{-1}\boldsymbol{\epsilon}_{k|k-1} - \frac{1}{2}\sum_{k=1}^{K}\log|\mathrm{H}_k\mathrm{X}_{k|k-1}\mathrm{X}_{k|k-1}^T\mathrm{H}_k^T + \mathrm{R}|, \tag{38}$$

where $\boldsymbol{\epsilon}_{k|k-1} = \boldsymbol{y}_k - \mathrm{H}_k\bar{\boldsymbol{x}}_{k|k-1} - \boldsymbol{b}$. We seek the value of α that maximizes the logarithm of the likelihood $\log p(\boldsymbol{y}_{1:K}|\alpha)$ in equation (38). The optimal value of α would yield the sequence of the observations $\boldsymbol{y}_{1:K}$ with a higher plausibility than any other possible values of α.

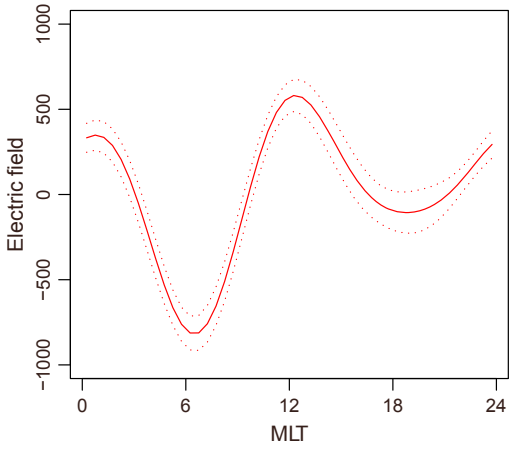

Figure 10. Estimated azimuthal profile of the eastward electric field at $L = 3.5$ at 1004 UT on 20 June 2001.

4. Validation Using Synthetic Data

We evaluate the proposed technique experimentally using a data set of synthetic EUV images. The synthetic EUV images were generated from a modeled plasmasphere obtained using a numerical model of the plasmasphere by *Ober et al.* [1997]. Figure 1 shows the evolution of the helium ion distribution obtained using this model under a certain electric potential pattern which is assumed to be the truth in this experiment. The polar cap potential drop Φ_0 was assumed to be the same as those on 20 June 2001, which will be examined in the next section. The color codes indicate the helium ion density distribution, and the white lines indicate the electric potential contours with intervals of 5 kV. Figure 2 shows the synthetic EUV image obtained from the ion distribution in Figure 1. This synthetic EUV image was generated according to equation (7) except that we added weak background noise and Poisson noises as the observation noises. The power law exponent in equation (2), α, was assumed to be 2. The orbit of the satellite was assumed to be the same as those on 20 June 2001. Although Figure 2 shows images taken at intervals of approximately 1 h, we used a sequence of synthetic EUV images taken at intervals of approximately 30 min from 0832 UT. Although the IMAGE satellite actually acquired EUV images at intervals of about 10 min, the use of the EUV images of every 10 min did not make a significant improvement on the result. We thus used the EUV images of every 30 min in the present paper. The model was initialized at 0832 UT using the estimate of the ion density obtained by linear inversion, as described in section 3.4. The synthetic images were then incorporated into the model at intervals of approximately 30 min. Since we did not use pixels for which the lines of sight pass below an altitude of 1500 km, as described above, we did not calculate the line of sight integral for such pixels in the synthetic data. For this reason, the pixels around the Earth are blank in Figure 2.

Figure 3 shows the estimation result. The color codes indicate the estimated equatorial helium ion density distribution. The white lines indicate the estimated electric potential contours with intervals of 5kV. Figure 4 shows the absolute values of the difference between the model in Figure 1 and the estimate in Figure 3. Figure 3 well reproduced the feature of the "true" helium ion density in Figure 1. The electric potential distribution was also successfully estimated. Since the shape of the plasmasphere observed by the IMAGE satellite would be sensitive to the electric field around the plasmapause, the estimate of the electric field should be most reliable near the plasmapause. Figure 5 shows the azimuthal distribution of the east-west electric field at $L = 3.5$ near the plasmapause. Positive values indicate an eastward electric field, and negative values indicate a westward electric field. The blue line indicates the "true" electric field distribution. The red solid line indicates the estimate, and the two thin dotted lines indicate the 2σ range of the uncertainty. The electric field was successfully estimated by the ETKF. Figure 6 shows the logarithm of the likelihood defined in equation (38) as a function of α. As described above, the likelihood indicates the probability that the sequence of the observed data are yielded from the given probability density function. Since it is rare that the exact same sequence will be observed again, the value of the likelihood typically becomes very small. Accordingly, the logarithm of the likelihood takes a large negative value. The likelihood was maximum at $\alpha = 2$, which means the optimal value of α is 2. As

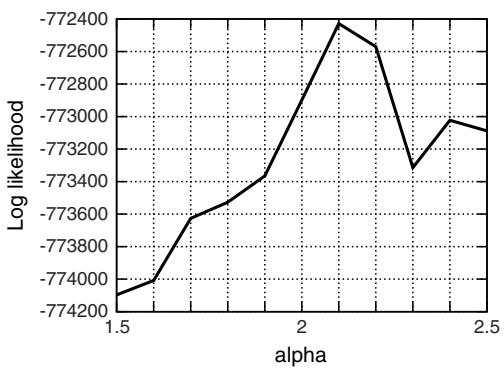

Figure 11. Log likelihood with respect to α for the event of 20 June 2001.

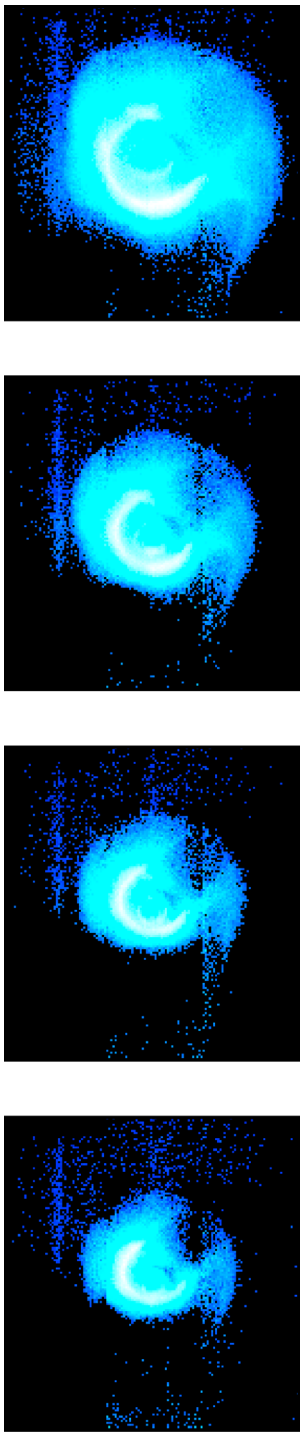

Figure 12. Sequence of EUV images for the event of 11 August 2000.

described above, this synthetic EUV image was generated under the assumption of $\alpha = 2$. The value of α was successfully estimated based on the likelihood.

5. Result and Discussion

Next, we demonstrate applications using real IMAGE/EUV data for two real cases as follows.

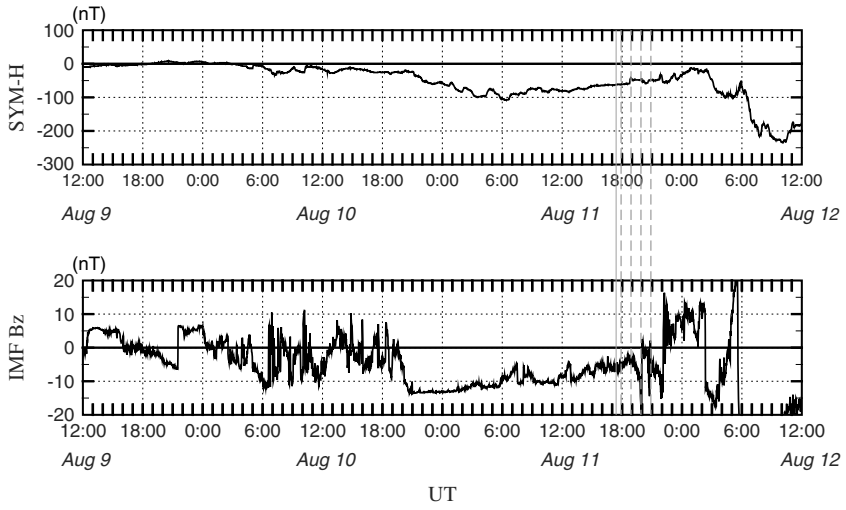

Figure 13. *SYM-H* index and the north-south component of the IMF from 12 UT on 9 August 2000 to 12 UT on 12 August 2000. The times at which the EUV images in Figure 12 were taken are indicated with vertical dashed lines.

5.1. Event on 20 June 2001

Figure 7 shows a sequence of EUV images taken by the IMAGE satellite on 20 June 2001, which is the same event examined in the companion paper [*Nakano et al.*, 2014]. Figure 8 shows the *SYM-H* index and the north-south component of the IMF in GSM coordinates from 0 UT on 18 June 2001 to 0 UT on 21 June 2001. The images in Figure 7 were taken during the recovery phase of a weak magnetic storm, during which the *Dst* index was minimized at −61 nT at 8 UT on 18 June, which was approximately 2 days earlier.

Figure 9 shows the estimated helium ion density distribution on the equatorial plane by means of color codes. The estimated electric potential distribution is also plotted with white lines with contour intervals of 5kV. In this event, an azimuthal density jump referred to as a shoulder [e.g., *Burch et al.*, 2001a] appeared at the dawn in Figure 7. Accordingly, in the estimate of Figure 9, the plasma in the postdawn was eroded, and the azimuthal density gradient developed around the dawn. *Goldstein et al.* [2002] suggested that the shoulder structure can be produced by the shielding electric field, which acts to reduce the electric field in the inner magnetosphere. Figure 10 shows the azimuthal profile of the estimated east-west electric field at $L = 3.5$. Again, positive values indicate an eastward electric field, and negative values indicate a westward electric field. A strong westward electric field was observed around the dawn. This westward electric field can be formed as a result of the shielding effect [e.g., *Jaggi and Wolf*, 1973; *Ebihara and Fok*, 2004]. Figure 11 shows the logarithm of the likelihood in equation (38) with respect to the power law exponent α. The likelihood was calculated using the data for the period from 9 UT to 15 UT during this event. The likelihood was maximized at $\alpha = 2.1$. This value appears to be reasonable in comparison with preceding studies on the power law exponent α [e.g., *Denton et al.*, 2006].

5.2. Event on 11 August 2000

Figure 12 shows a sequence of EUV images obtained from the IMAGE satellite in the event on 11 August 2000, which was also examined in the companion paper. Figure 13 shows the *SYM-H* index and the north-south component of the IMF in GSM coordinates from 12 UT on 9 August 2000 to 12 UT on 12 August 2000. The images in Figure 12 were taken approximately 10 h after the main phase of a magnetic storm. However, the IMF remained mostly southward until 22 UT. Hence, the convection was expected to be maintained during this period.

Figure 14 shows the result of the estimation. The color codes indicate the spatial distribution of the equatorial helium ion density, and the white lines indicate the electric potential contours. The contour intervals are 5 kV again. The result indicates that the helium ion plasmasphere roughly corotates with the Earth. In addition, the electric field tends to be weaker around the premidnight in the estimated electric potential pattern. This electric potential pattern might also be related to the shielding effect. In Figure 15, the azimuthal profile of the estimated eastward electric field at $L = 3.5$ is shown. The pattern indicates a noon-to-midnight

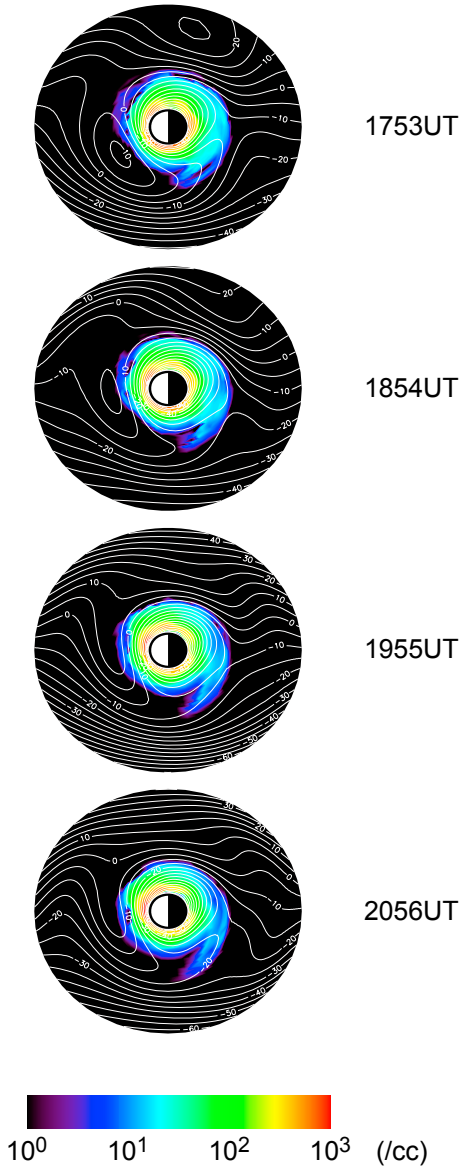

Figure 14. Estimated evolution of the helium ion distribution (color code) and the electric potential distribution (white lines) on 11 August 2000.

electric field rather than a dawn-to-dusk electric field. This feature might suggest the modulation of the external electric field due to some process in the inner magnetosphere. Figure 16 shows the logarithm of the likelihood with respect to the power law exponent α. The likelihood was calculated using the data for the period from 18 UT to 21 UT during this event. The likelihood was maximized at $\alpha = 2.0$, which is similar to that in the previous event on 20 June 2001. In Figure 11, the likelihood was multimodal, and the peak was less sharp. The difference in the log likelihood between the case of $\alpha = 2.1$ and the case of $\alpha = 1.6$ was approximately 1600. On the other hand, in Figure 16, the likelihood was unimodal and the difference in the log likelihood between the case of $\alpha = 2.0$ and the case of $\alpha = 1.5$ was about 3600 even though the data for shorter period were used for calculating the likelihood. This would suggest that the event of 11 August 2000 was preferable to the event of 20 June 2001 for determining α. On 20 June 2001, the satellite was located around the apogee from 10 UT to 12 UT, and its position moved only slightly during that period. As described above, the estimation of α is based on the change in the position of the satellite. Thus, when the satellite was near the apogee, the image data for a longer time might be required in order to obtain a reasonable estimate for α.

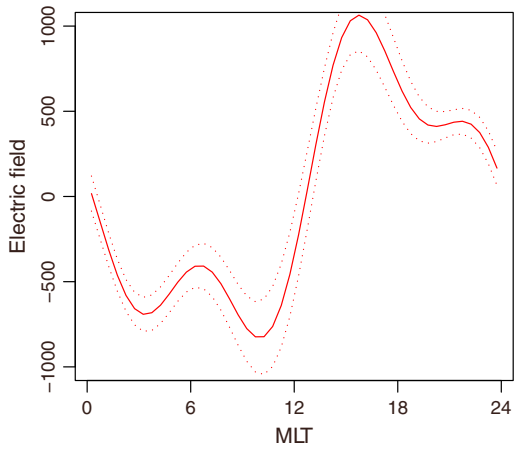

Figure 15. Estimated azimuthal profile of the eastward electric field at $L = 3.5$ at 1854 UT on 11 August 2000.

6. Concluding Remarks

We have developed a technique for estimating the temporal evolution of the helium ion distribution of the plasmasphere using IMAGE/EUV data. In the proposed technique, the initial state of the helium ion density distribution of the plasmasphere is estimated from a single snapshot of the EUV imaging data. The temporal evolution of the helium ion density distribution is then estimated from a sequence of IMAGE/EUV data using the ETKF. Although averaged features of the plasmasphere have been examined in a number of studies, reference information on the ion density was not available for each specific event. The data assimilation of the global EUV measurement offers the possibility of obtaining the temporal and spatial density distribution of plasmaspheric helium ions for specific events.

Assuming that the temporal evolution of the helium ion density distribution is primarily controlled by the electric field in the inner magnetosphere, we can also estimate the electric field around the plasmapause. Since the electric field is a crucial factor that controls the dynamics of charged particles, the estimates of the electric field would also provide a significant reference for discussing the mechanism of various phenomena in the inner magnetosphere. In our previous study [*Nakano et al.*, 2008], we demonstrated that the electric potential can be estimated by assimilating the energetic neutral atoms (ENAs) data into a dynamic model of the ring current ions. Since the ring current is typically located outside the plasmasphere, the ENA data and the EUV data are expected to be complementary to each other for the estimation of the electric field. As such, we plan to combine these two data assimilation techniques in the future, which could reinforce the estimation of the electric potential by each of the two techniques.

The estimation of the electric field has also been done by several previous works [e.g., *Goldstein et al.*, 2004, 2005; *Gallagher and Adrian*, 2007]. In contrast with these previous works, the proposed technique estimates the temporal evolution of the helium ion density distribution and the electric potential distribution simultaneously using the data assimilation approach. It thus provides a comprehensive picture of the evolution of the helium plasmasphere. The present framework also offers the prospect for determining the parameter for the density profile along the magnetic field line. Since the EUV images were taken from different directions due to the motion of the IMAGE satellite, we could obtain the information on the structure along the field line in addition to the two-dimensional structure on the equatorial plane. The proposed technique enables us to estimate the parameter for the density profile by considering both the motion of the spacecraft and the temporal evolution of the plasmasphere driven by the electric field. Using a maximum likelihood approach, we attempted to estimate the value of α, which is the power law exponent of the helium density profile along the field line. The power law exponent α was estimated as approximately 2 for the two events examined in the present paper, which appears to be consistent with previous studies. However, the uncertainty of the estimate appeared to be larger when the satellite was near apogee.

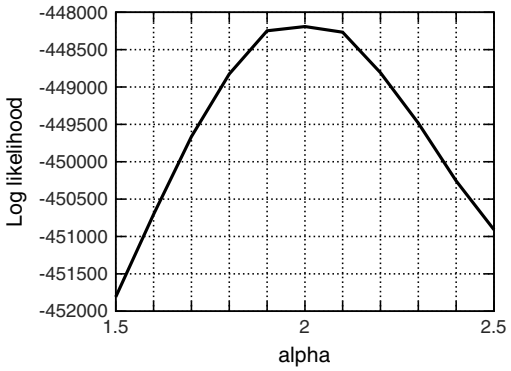

Figure 16. Log likelihood with respect to α for the event of 11 August 2000.

Acknowledgments
The authors would like to thank B.R. Sandel and the University of Arizona for providing the IMAGE/EUV data. The SOHO/SEM data were provided by the Space Science Center of University of Southern California. The authors would also like to thank N. Ness and the ACE Science Center for providing the ACE data. The *SYM-H* and *Dst* indices were provided by the World Data Center for Geomagnetism, Kyoto University. The present study was supported by the Japan Society for the Promotion of Science through a Grant-in-Aid for Young Scientists (B), 24740334, and was partially supported by Young Researcher Overseas Visit Program of the Graduate University for Advanced Studies.

Michael Liemohn thanks Jerry Goldstein and another reviewer for their assistance in evaluating this paper.

References

Anderson, J. L., and S. L. Anderson (1999), A Monte Carlo implementation of the nonlinear filtering problem to produce ensemble assimilations and forecasts, *Mon. Weather Rev.*, *127*, 2741–2758.
Bishop, C. H., R. J. Etherton, and S. J. Majumdar (2001), Adaptive sampling with the ensemble transform Kalman filter. Part I: Theoretical aspects, *Mon. Weather Rev.*, *129*, 420–436.
Boudarie, S. A., and V. F. Maget (2012), Electron radiation belt data assimilation with an ensemble Kalman filter relying on the Salammbô code, *Ann. Geophys.*, *30*, 929–943.
Burch, J. L., D. G. Mitchell, B. R. Sandel, P. C. Brandt, and M. Wüest (2001a), Global dyamics of the plasmasphere and ring current during magnetic storms, *Geophys. Res. Lett.*, *28*, 1159–1162.
Burch, J. L., et al. (2001b), Views of Earth's magnetosphere with the IMAGE satellite, *Science*, *291*, 619–624.
Cohn, S. E., N. S. Sivakumaran, and R. Todling (1994), A fixed-lag smoother for retrospective data assimilation, *Mon. Weather Rev.*, *122*, 2838–2867.
Denton, R. E., K. Takahashi, I. A. Galkin, P. A. Nsumei, X. Huang, B. W. Reinisch, R. R. Anderson, M. K. Sleeper, and W. J. Hughes (2006), Distribution of density along magnetospheric field lines, *J. Geophys. Res.*, *111*, A04213, doi:10.1029/2005JA011414.
Ebihara, Y., and M.-C. Fok (2004), Postmidnight storm-time enhancement of tens-of-keV proton flux, *J. Geophys. Res.*, *109*, A12209, doi:10.1029/2004JA010523.
Evensen, G. (1994), Sequential data assimilation with a nonlinear quasi-geostrophic model using Monte Carlo methods to forecast error statistics, *J. Geophys. Res.*, *99*(C5), 10,143–10,162.
Evensen, G. (2003), The ensemble Kalman filter: Theoretical formulation and practical implementation, *Ocean Dyn.*, *53*, 343–367.
Evensen, G., and P. J. van Leeuwen (2000), An ensemble Kalman smoother for nonlinear dynamics, *Mon. Weather Rev.*, *128*, 1852–1867.
Fok, M.-C., R. A. Wolf, R. W. Spiro, and T. E. Moore (2001), Comprehensive computational model of Earth's ring current, *J. Geophys. Res.*, *104*, 8417–8424, doi:10.1029/2000JA000235.
Gallagher, D. L., and M. L. Adrian (2007), Two-dimensional drift velocities from the IMAGE EUV plasmaspheric imager, *J. Atmos. Sol. Terr. Phys.*, *69*, 341–350.
Gallagher, D. L., M. L. Adrian, and M. W. Liemohn (2005), Origin and evolution of deep plasmaspheric notches, *J. Geophys. Res.*, *110*, A09201, doi:10.1029/2004JA010906.
Galvan, D. A., M. B. Moldwin, B. R. Sandel, and G. Crowley (2010), On the causes of plasmaspheric rotation variability: IMAGE EUV observations, *J. Geophys. Res.*, *115*, A01214, doi:10.1029/2009JA014321.
Goldstein, J., R. W. Spiro, P. H. Reiff, R. A. Wolf, B. R. Sandel, J. W. Freeman, and R. L. Lambour (2002), IMF-driven overshielding electric field and the origin of the plasmaspheric shoulder of May 24, 2000, *Geophys. Res. Lett.*, *29*(16), 1819, doi:10.1029/2001GL014534.
Goldstein, J., R. A. Wolf, B. R. Sandel, and P. H. Reiff (2004), Electric fields deduced from plasmapause motion in IMAGE EUV images, *Geophys. Res. Lett.*, *31*, L01801, doi:10.1029/2003GL018797.
Goldstein, J., J. L. Burch, B. R. Sandel, S. B. Mende, P. C. son Brandt, and M. R. Hairston (2005), Coupled response of the inner magnetosphere and ionosphere on 17 April 2002, *J. Geophys. Res.*, *110*, A03205, doi:10.1029/2004JA010712.
Hoffman, J. H., and W. H. Dodson (1980), Light ion concentrations and fluxes in the polar regions during magnetically quiet times, *J. Geophys. Res.*, *85*, 626–632.
Jaggi, R. K., and R. A. Wolf (1973), Self-consistent calculation of the motion of a sheet of ions in the magnetosphere, *J. Geophys. Res.*, *78*, 2852–2866.
Jorgensen, A. M., D. Ober, J. Koller, and R. H. W. Friedel (2011), Specification of the Earth's plasmasphere with data assimilation, *Adv. Space Res.*, *47*, 2152–2161.
Kalman, R. E. (1960), A new approach to linear filtering and prediction problems, *Trans. ASME J. Basic Eng.*, *82*, 35–45.
Kalnay, E. (2003), *Atmospheric Modeling, Data Assimilation and Predictability*, Cambridge Univ. Press, Cambridge, U. K.
Kitagawa, G. (2010), *Introduction to Time Series Modeling*, Chapman and Hall/CRC, London, U. K.
Koller, J., Y. Chen, G. D. Reeves, R. H. W. Friedel, T. E. Cayton, and J. A. Vrugt (2007), Identifying the radiation belt source region by data assimilation, *J. Geophys. Res.*, *112*, A06244, doi:10.1029/2006JA012196.
Kondrashov, D., Y. Shprits, M. Ghil, and R. Thorne (2007), A Kalman filter technique to estimate relativistic electron lifetimes in the outer radiation belt, *J. Geophys. Res.*, *112*, A10227, doi:10.1029/2007JA012583.
Liemohn, M. W., A. J. Ridley, D. L. Gallagher, D. M. Ober, and J. U. Kozyra (2004), Dependence of plasmaspheric morphology on the electric field description during the recovery phase of the 17 April 2002 magnetic storm, *J. Geophys. Res.*, *109*, A03209, doi:10.1029/2003JA010304.
Liemohn, M. W., A. J. Ridley, P. C. Brandt, D. L. Gallagher, J. U. Kozyra, D. M. Ober, D. G. Mitchell, E. C. Roelof, and R. DeMajistre (2005), Parametric analysis of nightside conductance effects on inner magnetospheric dynamics for the 17 April 2002 storm, *J. Geophys. Res.*, *110*, A12S22, doi:10.1029/2005JA011109.
Livings, D. M., S. L. Dance, and N. K. Nichols (2008), Unbiased ensemble square root filters, *Physica D*, *237*, 1021–1028.
Matsui, H., V. K. Jordanova, J. M. Quinn, and R. B. Torbert (2004), Derivation of electric potential patterns in the inner magnetosphere from Cluster EDI data: Initial results, *J. Geophys. Res.*, *109*, A10202, doi:10.1029/2003JA010319.
Matsui, H., R. B. Torbert, H. E. Spence, Y. V. Khotyaintsev, and P.-A. Lindqvist (2013), Revision of empirical electric field modeling in the inner magnetosphere using Cluster data, *J. Geophys. Res. Space Physics*, *118*, 4119–4134, doi:10.1002/jgra.50373.
Menk, F. W., D. Orr, M. A. Clilverd, A. J. Smith, C. L. Waters, D. K. Milling, and B. J. Fraser (1999), Monitoring spatial and temporal variations in the dayside plasmasphere using geomagnetic field line resonances, *J. Geophys. Res.*, *104*, 19,955–19,969.
Murakami, G., M. Hirai, and I. Yoshikawa (2007), The plasmaspheric response to the southward turning of the IMF derived from sequential EUV images, *J. Geophys. Res.*, *112*, A06217, doi:10.1029/2006JA012174.
Naehr, S. M., and F. R. Toffoletto (2005), Radiation belt data assimilation with an extended Kalman filter, *Space Weather*, *3*, S06001, doi:10.1029/2004SW000121.
Nakano, S., G. Ueno, Y. Ebihara, M.-C. Fok, S. Ohtani, P. C. Brandt, D. G. Mitchell, K. Keika, and T. Higuchi (2008), A method for estimating the ring current structure and the electric potential distribution using ENA data assimilation, *J. Geophys. Res.*, *113*, A05208, doi:10.1029/2006JA011853.
Nakano, S., et al. (2014), Estimation of the helium ion density distribution in the plasmasphere based on a single IMAGE/EUV image, *J. Geophys. Res. Space Physics*, doi:10.1002/2013JA019733.
Nishida, A. (1966), Formation of plasmapause, or magnetospheric plasma knee, by the combined action of magnetospheric convection and plasma escape from the tail, *J. Geophys. Res.*, *71*, 5669–5679.
Obana, Y., F. W. Menk, and I. Yoshikawa (2010), Plasma refilling rates for $L = 2.3$–3.8 flux tubes, *J. Geophys. Res.*, *115*, A03204, doi:10.1029/2009JA014191.

Ober, D. M., J. L. Horwitz, and D. L. Gallagher (1997), Formation of density troughs embedded in the outer plasmasphere by subauroral ion drift events, *J. Geophys. Res.*, *102*, 14,595–14,602.

Park, C. G. (1974), Some features of plasma distribution in the plasmasphere deduced from Antarctic whistlers, *J. Geophys. Res.*, *79*, 169–173.

Pierrard, V., G. V. Khazanov, J. Cabrera, and J. Lemaire (2008), Influence of the convection electric field models on predicted plasmapause positions during magnetic storms, *J. Geophys. Res.*, *113*, A08212, doi:10.1029/2007JA012612.

Reinisch, B. W., M. B. Moldwin, R. E. Denton, D. L. Gallagher, H. Matsui, V. Pierrard, and J. Tu (2009), Augmented empirical models of plasmaspheric density and electric field using IMAGE and CLUSTER data, *Space Sci. Rev.*, *145*, 231–261.

Sakov, P., and P. R. Oke (2008), Implications of the form of the ensemble transformation in the ensemble square root filters, *Mon. Weather Rev.*, *136*, 1042–1053.

Sandel, B. R., et al. (2000), The extreme ultraviolet imager investigation for the IMAGE mission, *Space Sci. Rev.*, *91*, 197–242.

Vasyliunas, V. M. (1970), Mathematical models of magnetospheric convection and its coupling to the ionosphere, in *Particles and Fields in the Magnetosphere*, edited by B. M. McCormac, pp. 60–71, D. Reidel, Dordrecht, Netherlands.

Vasyliunas, V. M. (1972), The interrelationship of magnetospheric process, in *Earth's Magnetospheric Process*, edited by McCormac, B. M., pp. 29–38, D. Reidel, Dordrecht, Holland.

Wang, X., C. H. Bishop, and S. J. Julier (2004), Which is better, an ensemble of positive-negative pairs or a centered spherical simplex ensemble?, *Mon. Weather Rev.*, *132*, 1590–1605.

Weimer, D. R. (2001), An improved model of ionospheric electric potentials including substorm perturbations and application to the Geospace Environment Modeling November 24, 1996 event, *J. Geophys. Res.*, *106*, 407–416.